Supporting information for

Chiral Morphology in MoS_2 Nanostructures for Spin-Polarized Bifunctional Oxygen Electrocatalysis

Lorenzo Branzi,[a]* Fiham Fahim,[b]* Niccolò Giaconi,[c,d]* Lapo Querci,[c,d] Lorenzo Poggini,[c,d,e] Roberta Sessoli,[c,d] Matteo Mannini,[c,d] Aravind Vadakkayil,[b] Brian P. Bloom,[b] David H. Waldeck,[b#] and Yurii K. Gun'ko[a]*

a School of Chemistry, Trinity College Dublin,College Green, Dublin, Ireland.

b Chemistry Department, University of Pittsburgh, Pittsburgh, Pennsylvania 15260, USA.

c Department of Chemistry 'Ugo Schiff', University of Florence, 50019 Sesto Fiorentino (FI), Italy.

d INSTM Research Unit, University of Florence, 50121 Firenze (FI), Italy.

e ICCOM-CNR, 50019 Sesto Fiorentino (FI), Italy

[#] Deceased

E-mail: Branzil@tcd.ie, MOM143@pitt.edu, n.giaconi@nanogune.eu and igouko@tcd.ie

Downloaded from pubs.acs.org/ancac3/article-supplement/5429321/pdf/nn6c08876_si_001/ by CNR user on 21 September 2026

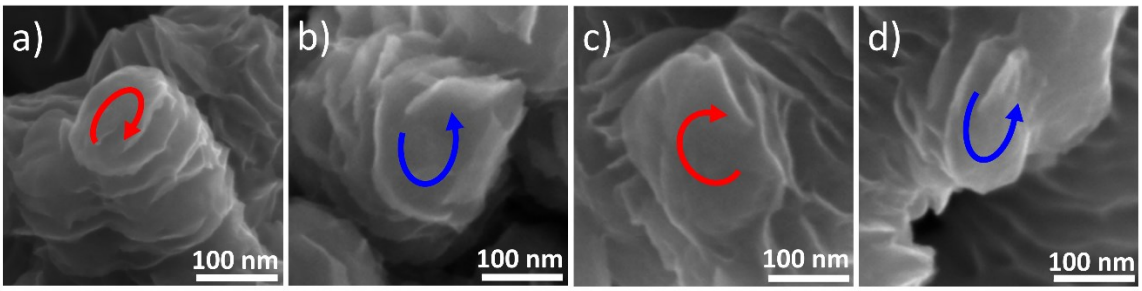

Figure S1. SEM images of Rac-MoS_2 nanosheets showing helices with different handedness.

Downloaded from pubs.acs.org/ancac3/article-supplement/5429321/pdf/nn6c08876_si_001/ by CNR user on 21 September 2026

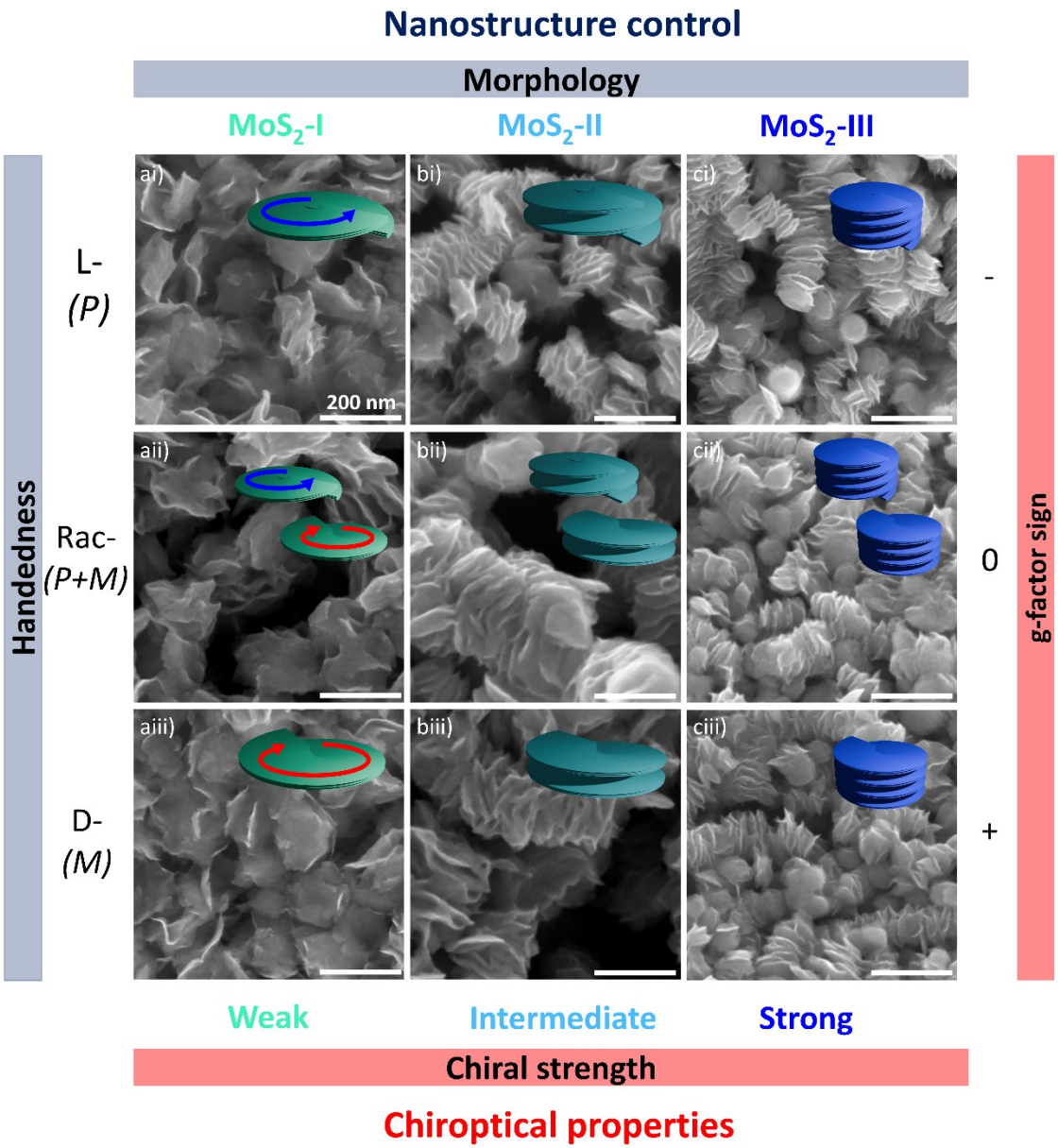

Figure S2. SEM images of MoS_2 nanosheets with different morphology and handedness, and the relative effect on the chiroptical properties in terms of chiral strength and g-factor sign.

Downloaded from pubs.acs.org/ancac3/article-supplement/5429321/pdf/nn6c08876_si_001/ by CNR user on 21 September 2026

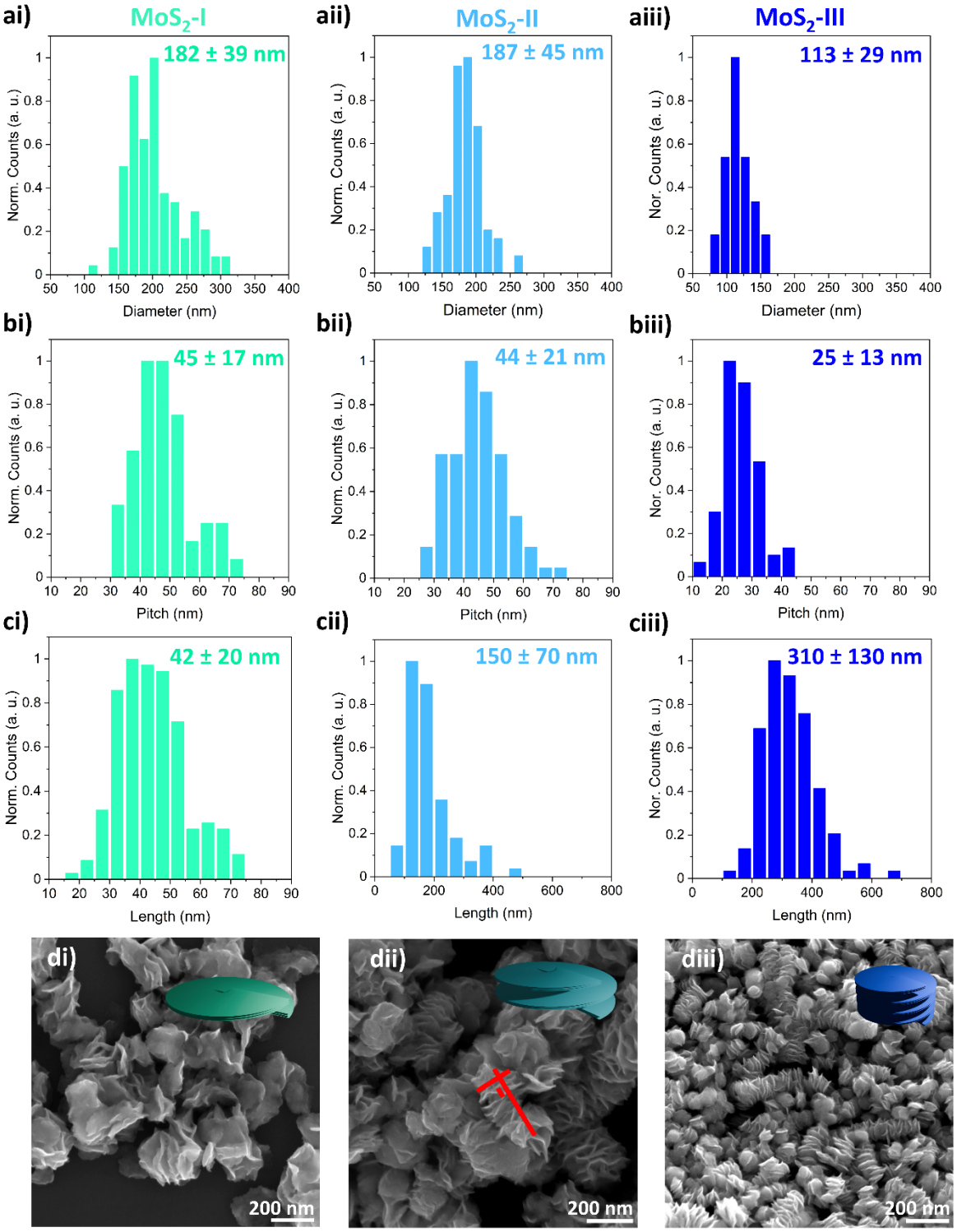

Figure S3. Size distribution histograms representing diameter (a), pitch (b) and length (c) of different helical MoS_2 nanosheets. d) SEM images highlighting an indicative example of diameter, pitch and length of the of MoS_2-I (i), MoS_2-II (i) and MoS_2-III (iii) helical nanosheets, respectively.

Downloaded from pubs.acs.org/ancac3/article-supplement/5429321/pdf/nn6c08876_si_001/ by CNR user on 21 September 2026

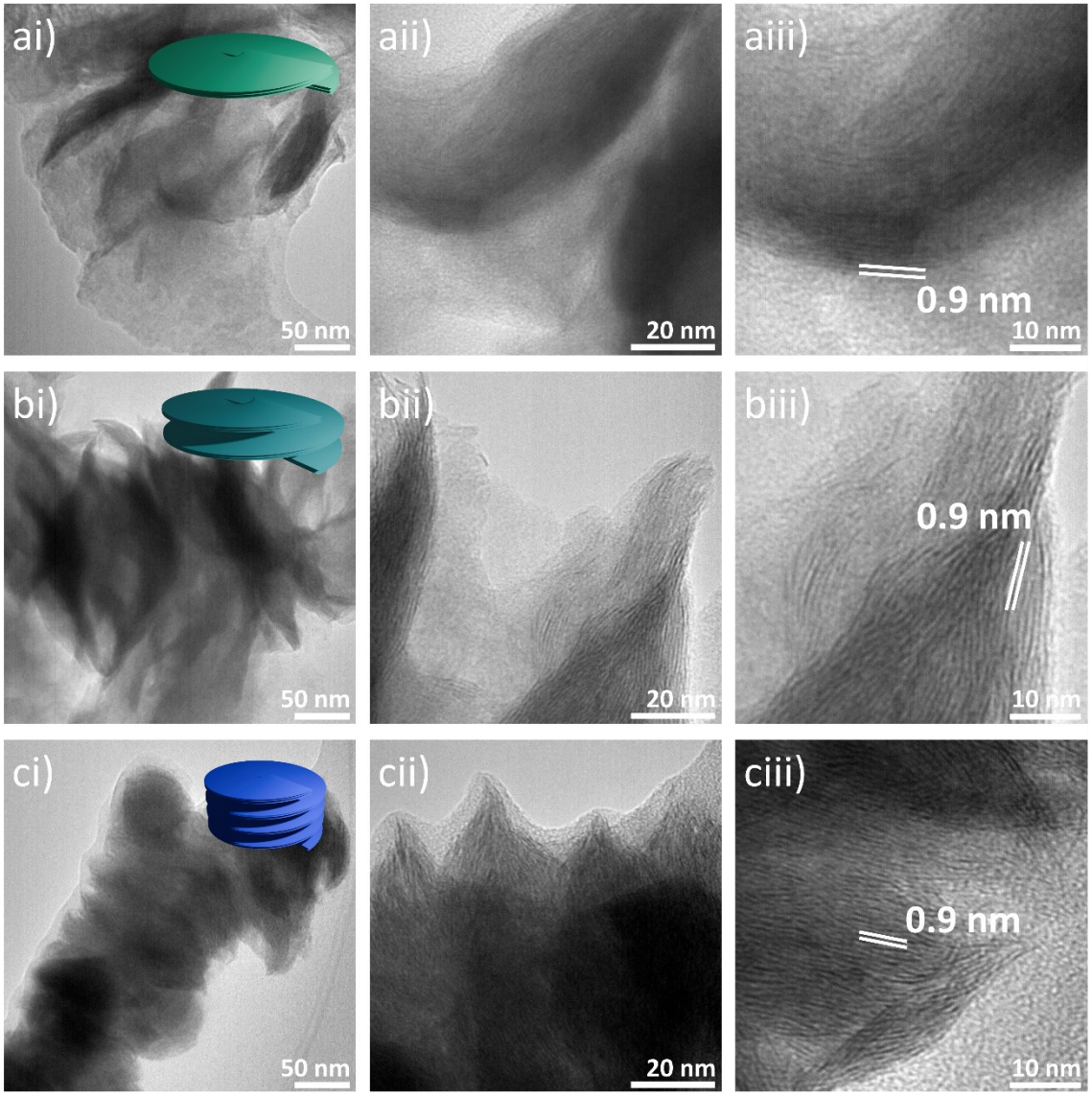

Figure S4. TEM and HR-TEM images of MoS_2-I (a), MoS_2-II (b) and MoS_2-III (c) nanosheets at different magnifications.

Downloaded from pubs.acs.org/ancac3/article-supplement/5429321/pdf/nn6c08876_si_001/ by CNR user on 21 September 2026

Table S1. Estimated 1T and 2H phases content based on the fitting of Mo 3d peaks.

Label	1T Integrated area	2H Integrated area	%1T	%2H
MoS_2-I	0.738	0.257	74.1	25.9
MoS_2-II	0.712	0.276	72.0	28.0
MoS_2-III	0.760	0.231	76.7	23.3

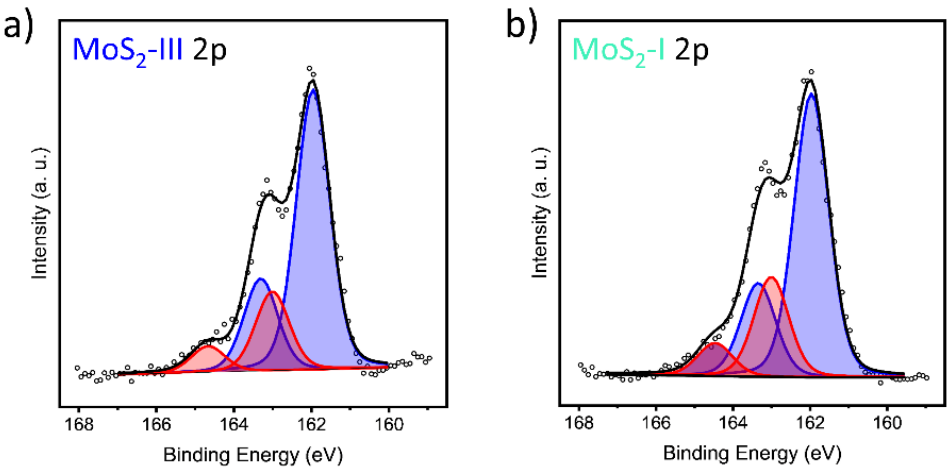

Figure S5. S 2*p* XPS spectra of MoS_2-III (a) and MoS_2-I (b). Experimental data are shown as dots and the composite spectrum is shown in black, the 1T and 2H doublet contributions are represented in blue and red, respectively.

Table S2. g-factor values at 220 nm of 1T-MoS_2 nanosheets with different chirality.

Label	TA Conc (mM)	L-MoS_2 g-factor	D-MoS_2 g-factor	[a]Rac-MoS_2 g-factor
MoS_2-I	10	-0.0023	0.0023	3.2×10^{-5}
MoS_2-II	25	-0.0063	0.0062	-5.0×10^{-5}
MoS_2-III	100	-0.0123	0.0118	-3.4×10^{-5}

[a] The g-factor values for Rac-nanosheets correspond to the noise of the CD measurement.

Downloaded from pubs.acs.org/ancac3/article-supplement/5429321/pdf/nn6c08876_si_001/ by CNR user on 21 September 2026

Spin transport measurements

Substrate preparation:

Substrates for both mc-AFM and EGaIn measurements were prepared by DC magnetron sputtering (Korvus technologies, HEX Series) followed by a template-stripping procedure (Figure S6). Gold (10 nm), nickel (100 nm), and titanium (10 nm) layers were sequentially deposited onto a silicon (100) wafer at a rate of 0.1 Å s^{-1}. Pre-cut glass slides (1x1 cm) were attached using an optical adhesive and cured under UV light. After lift-off, the resulting trimetallic substrates expose an atomically flat gold surface.

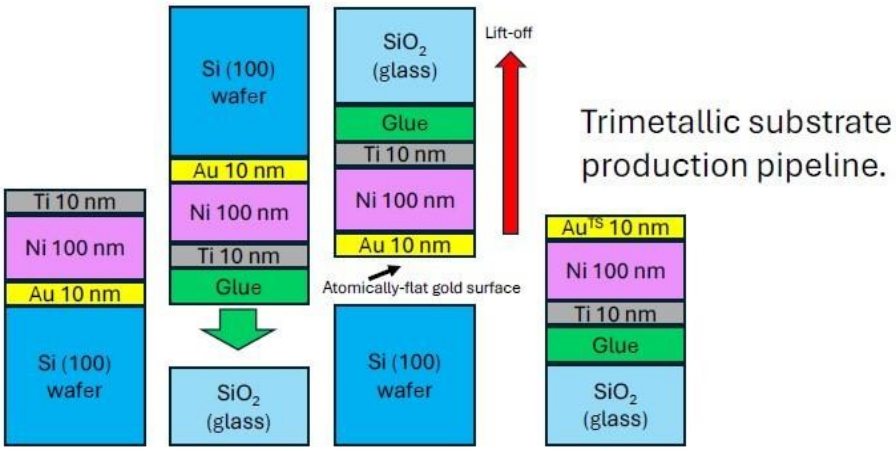

Figure S6. Template stripping procedure schematic.

Sample preparation:

Samples for both mc-AFM and EGaIn analyses were prepared by spin-coating (Figure S7). The nanosheets were dispersed in anhydrous ethanol (0.3 mg mL^{-1}) by ultrasonication (60 s). 200 µL of the suspension were deposited on the trimetallic substrate using a micro-pipette, followed by spin-coating (2000 rpm, 30 s; acceleration/deceleration 3 s each). Prior to measurements, the Ni domains of the substrate were magnetized either upward or downward using a 0.5 T static magnet.

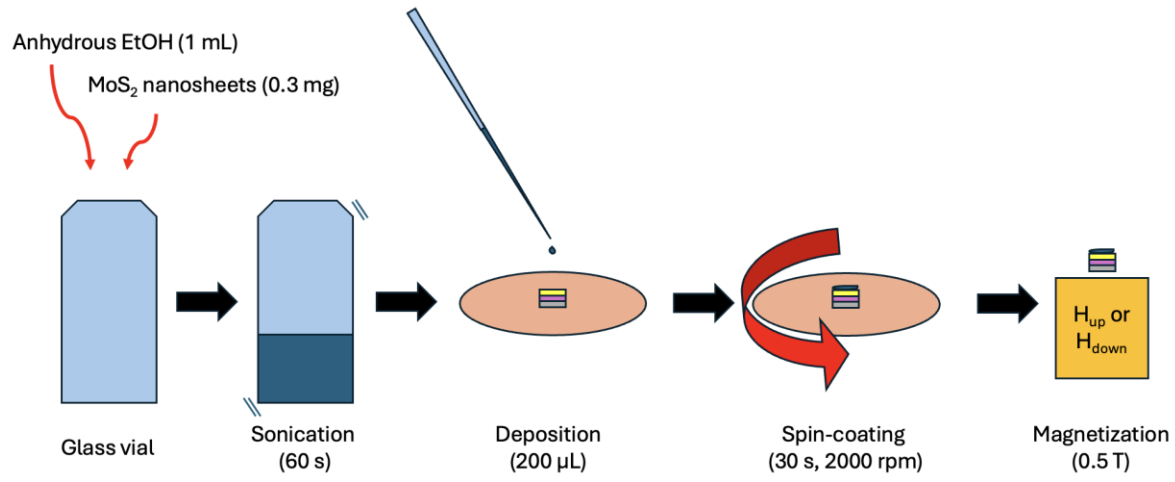

Figure S7. Schematic for the preparation of MoS_2 nanosheet layers and magnetization prior to mc-AFM and EGaIn measurements.

Downloaded from pubs.acs.org/ancac3/article-supplement/5429321/pdf/nn6c08876_si_001/ by CNR user on 21 September 2026

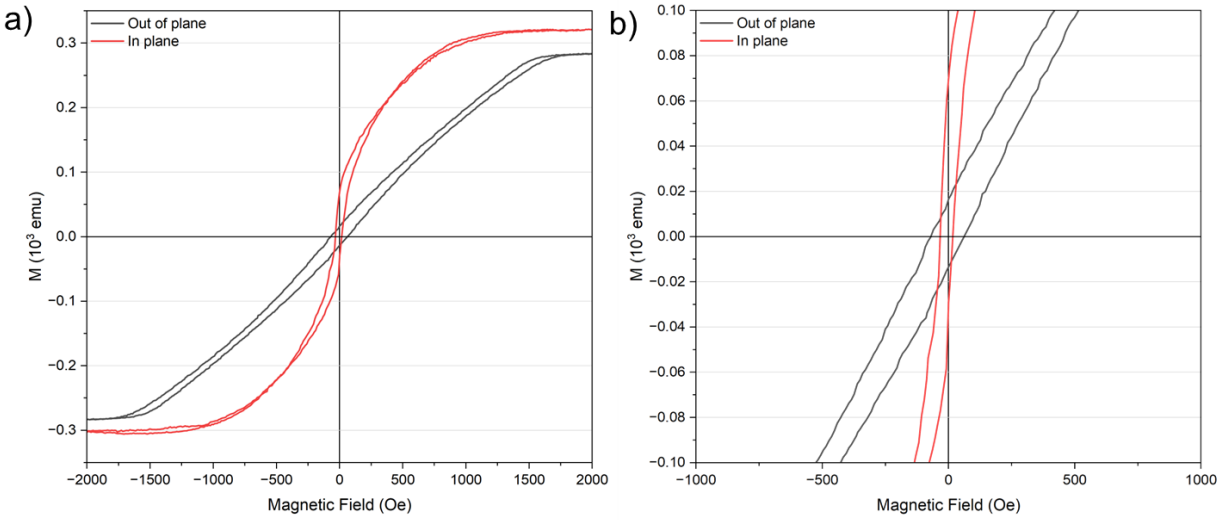

Figure S8. a) Magnetization curves acquired on the Au(10 nm)/Ni(100 nm)/Ti(10 nm) substrates used for the mc-AFM and EGaIn experiments applying an in-plane (red line) and an out-of-plane (black line) magnetic field. b) Magnification of the magnetization curves in the ±1000 Oe range.

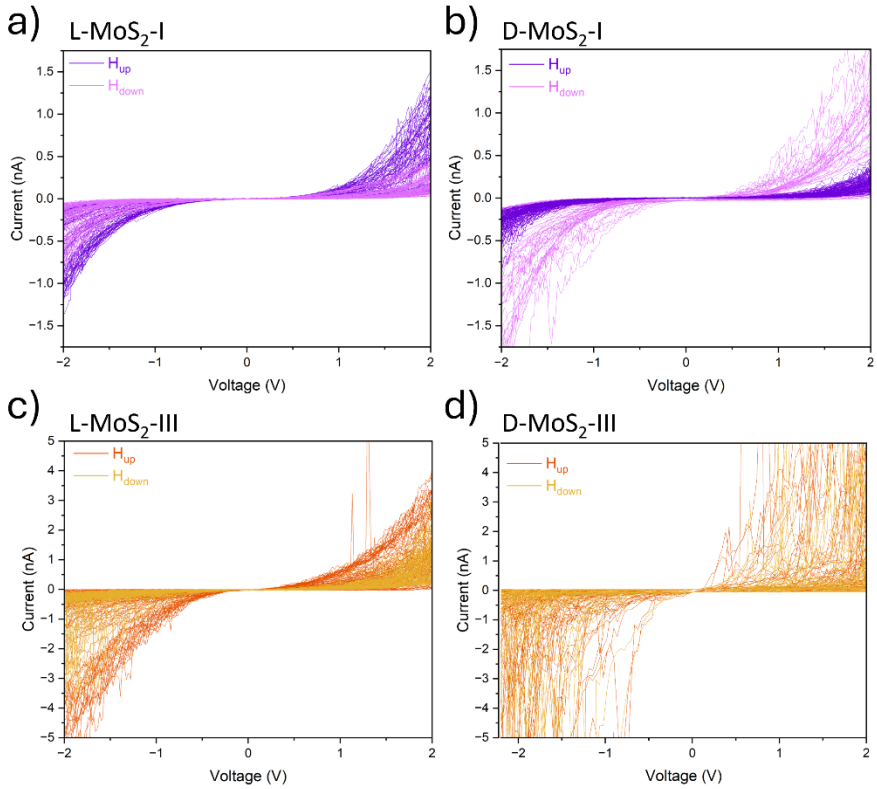

Figure S9. Raw mc-AFM measurements of L-MoS_2-I (a), D-MoS_2-I (b), L-MoS_2-III (c) and D-MoS_2-III (d) nanosheets.

Downloaded from pubs.acs.org/ancac3/article-supplement/5429321/pdf/nn6c08876_si_001/ by CNR user on 21 September 2026

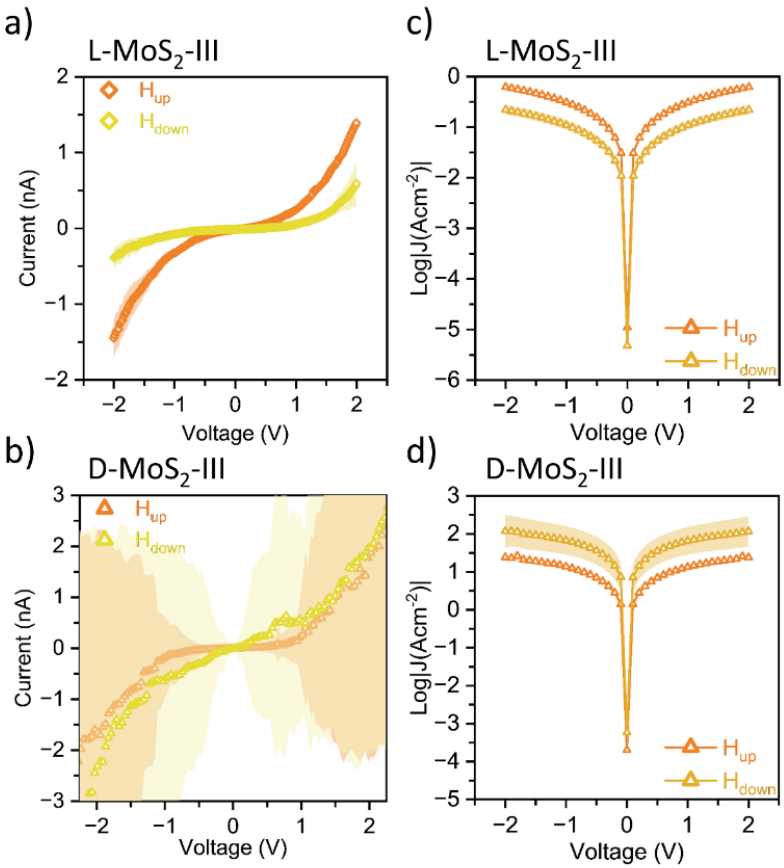

Figure S10. mc-AFM measurements of L-MoS_2-III (a) and D-MoS_2-III (b) nanosheets under different magnetizations. EGaIn measurements of L-MoS_2-III (c) and D-MoS_2-III (d) nanosheets under different magnetizations. The errors are represented as a shadow area behind the curves and in some cases, these are smaller than the symbol size

Downloaded from pubs.acs.org/ancac3/article-supplement/5429321/pdf/nn6c08876_si_001/ by CNR user on 21 September 2026

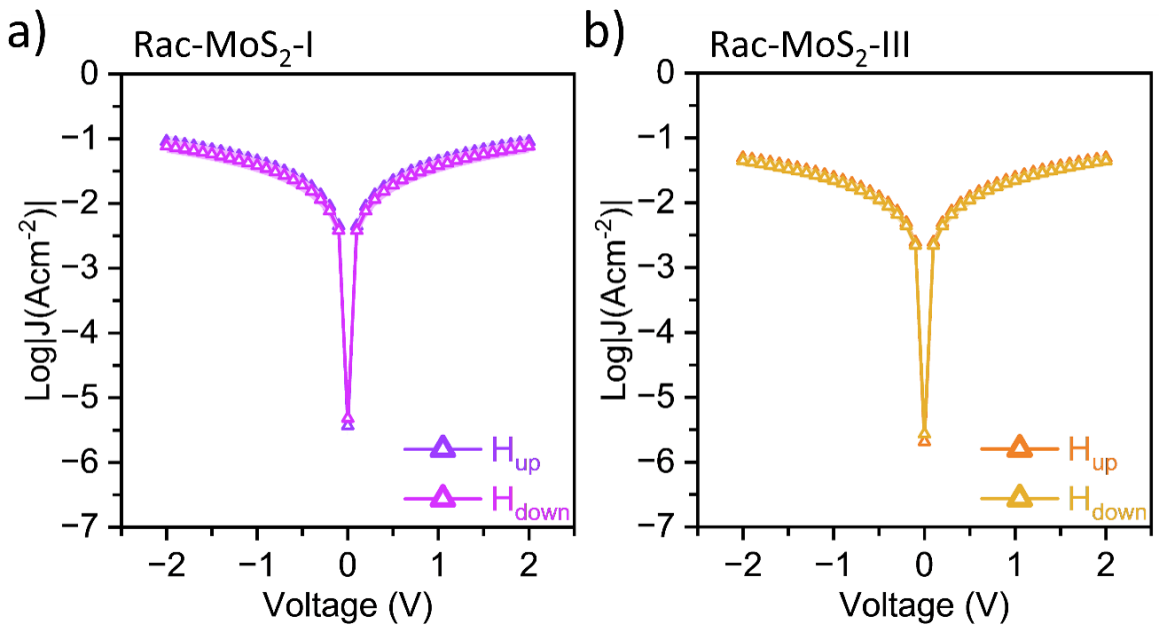

Figure S11. EGaIn measurements of Rac-MoS_2-I (a) and Rac-MoS_2-III (b) nanosheets under different magnetizations. The errors are represented as a shadow area behind the curves and in some cases, these are smaller than the symbol size

Downloaded from pubs.acs.org/ancac3/article-supplement/5429321/pdf/nn6c08876_si_001/ by CNR user on 21 September 2026

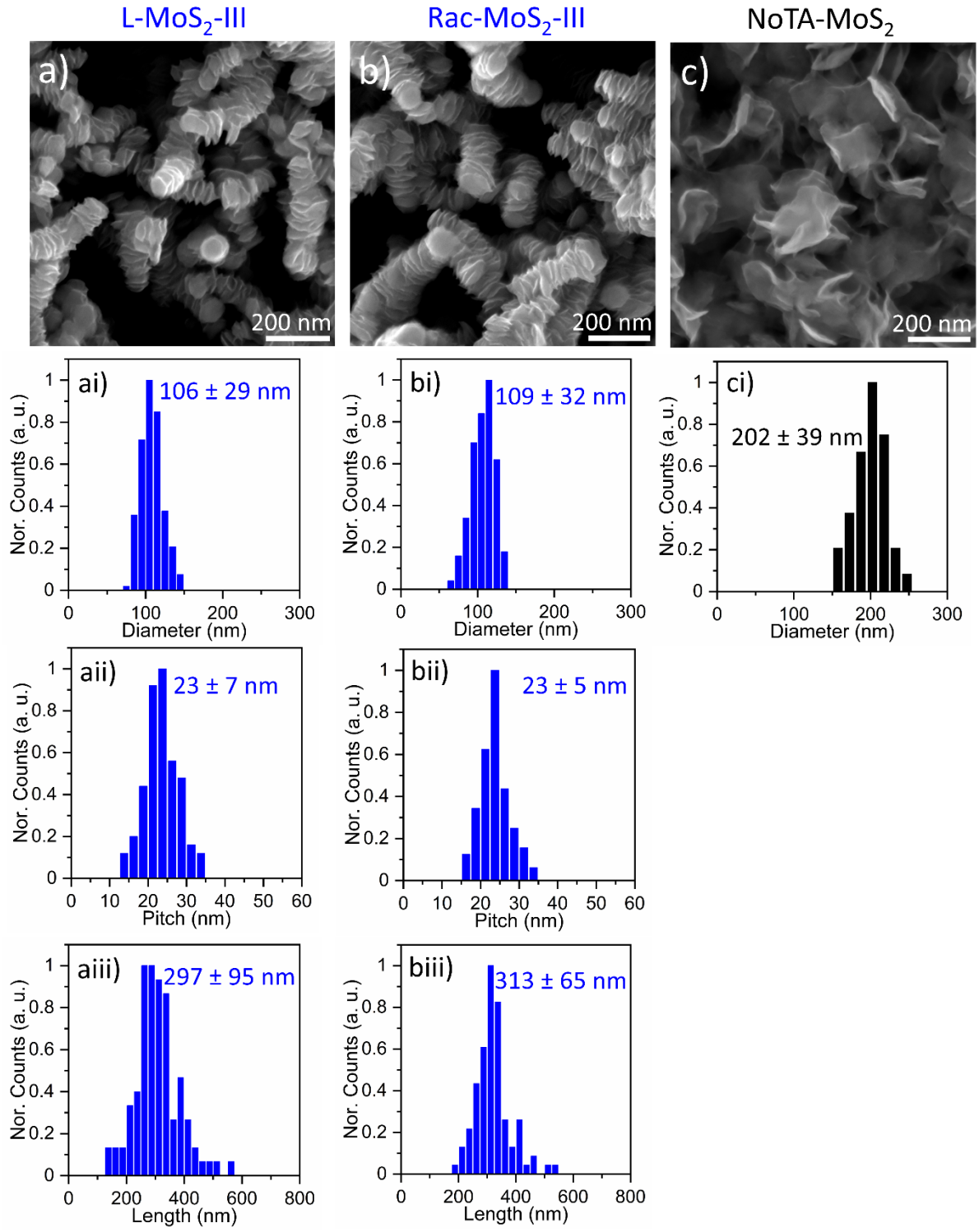

Figure S12. Analysis of the morphology chiral L-MoS_2-III nanosheets and the achiral controls Rac-MoS_2-III and NoTA-MoS_2 nanosheets. Representative SEM images are reported in panel a), b) and c) for L-MoS_2-III, Rac-MoS_2-III and NoTA-MoS_2, respectively. Size distribution histograms representing diameter (i), pitch (iii) and length (iii) for the different samples.

Downloaded from pubs.acs.org/ancac3/article-supplement/5429321/pdf/nn6c08876_si_001/ by CNR user on 21 September 2026

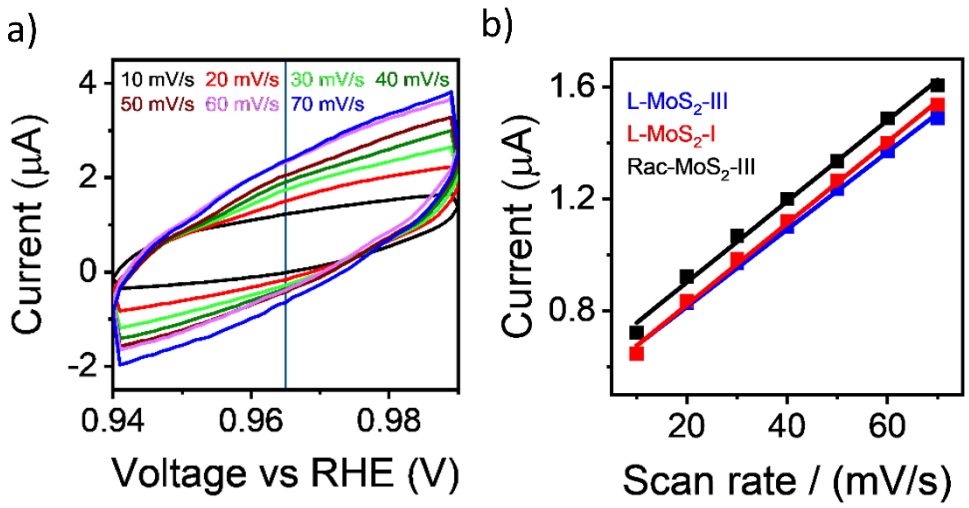

Figure S13. a) Representative cyclic voltammograms obtained for the L-MoS_2-III catalytic system in the non-Faradaic potential range of 0.99-0.94 V vs RHE at scan rates of 10, 20, 30, 40, 50, 60 and 70 mV/s. b) plot of current vs scan rate for the L-MoS_2-III (blue), L-MoS_2-I (red) and Rac- MoS_2-III (black) catalytic systems used to calculate the capacitance in the non-Faradaic region for ORR.

Table S3. Shows the ECSA values calculated for L-MoS_2-III, L-MoS_2-I and Rac-MoS_2-III catalytic systems. Each value represents the averages from three independently prepared electrodes.

Catalysts	**L-MoS_2-III**	**L-MoS_2-I**	**Rac-MoS_2-III**
ECSA / cm^2	0.35 ± 0.02	0.36 ± 0.02	0.37 ± 0.03

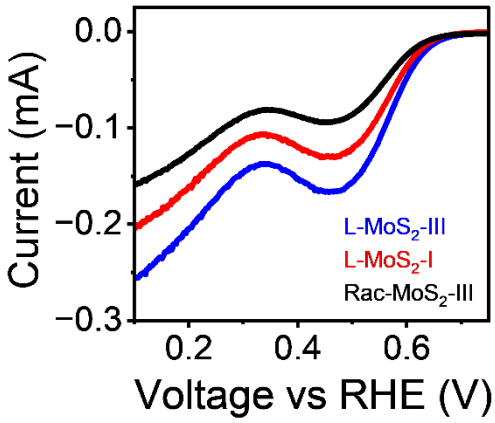

Figure S14. The current vs voltage linear sweep voltammograms at ORR potential conditions of L-MoS_2-III (blue), L-MoS_2-I (red), and Rac-MoS_2-III (black) catalysts in O_2 saturated 0.1 M KOH solutions at 1600 rpm.

Downloaded from pubs.acs.org/ancac3/article-supplement/5429321/pdf/nn6c08876_si_001/ by CNR user on 21 September 2026

Koutecky-Levich Analysis: Using a rotating-ring disk electrode, the Levich equation becomes applicable at steady state conditions, where the concentration of the reactant at the electrode surface is zero. In this limit, the diffusion rate of the reactant becomes equal to the convection rate of the rotating electrode.[62] The limiting current density $i_{L,0}$ under these conditions is given by the Levich equation:

$$i_{L,0} = 0.201nFD_O^{\frac{2}{3}}\nu^{\frac{-1}{6}}\omega^{\frac{1}{2}}C_O = K\omega^{\frac{1}{2}} \qquad eq.S1$$

$$K = 0.201nFD_O^{\frac{2}{3}}\nu^{\frac{-1}{6}}C_O \qquad eq.S2$$

where n is the total number of electrons, F is the Faraday's constant, and ω is the rotation speed of the working electrode (rpm). D_O, C_O and ν correspond to diffusion coefficient ($cm^2\ s^{-1}$) of O_2, concentration ($mol\ cm^{-3}$) of O_2, and kinematic viscosity ($cm^2\ s^{-1}$), respectively.

The Koutecky-Levich equation can be obtained by modifying the Levich equation with a kinetic component, $i_{k,O}$ which comes from the Butler-Volmer model equation:

$$\frac{1}{J} = \frac{1}{i_{L,O}} + \frac{1}{i_{k,O}} \qquad eq.S3$$

$$i_{k,O} = i_o exp\left(-\frac{(1-\alpha)nF\left(E-E_{eq}\right)}{RT}\right) \qquad eq.S4$$

where α is the charge transfer coefficient and i_o is the exchange current density. The applied potential and the equilibrium potential are represented by E and E_{eq}, respectively.

Eq. S5 is obtained is obtained by substituting eq S1 and S4 to eq S3:

$$\frac{1}{J} = \frac{\omega^{-1/2}}{K} + \frac{1}{i_o}exp\left(\frac{(1-\alpha)nF\left(E-E_{eq}\right)}{RT}\right) \qquad eq.S5$$

In the linear sweep voltammograms for the ORR, the potential range from 0.50-0.60 V exhibits a region where the electron transfer between the reactant and the electrode is the slow step. The current observed in the voltammogram depends on both the kinetic current generated due to the electron transfer and the current due to the diffusion of O_2 from the bulk. To construct the Koutecky-Levich plot (Figure S15), linear sweep voltammograms were obtained at different rotation rates of 400, 800, 1200, 1600 and 2000 rpm. The y-intercept of equation S6 gives $1/i_{k,o}$, from which the kinetic current density can be calculated. Figure S16 gives the plot of kinetic current density ($i_{k,O}$) against the potential for L-MoS_2-III, L-MoS_2-I and Rac-MoS_2-III nanosheets.

Finally, the exchange current density (i_0) and the charge transfer coefficient (α) were calculated according to eq. S6 by the plot shown in Figure 4b. The final values are reported in Table S4 for the case where $n = 2$ (the common choice for ORR) and $n = 1$.

$$E = -\frac{RT}{(1-\alpha)nF}ln\left(i_{k,O}\right) + E_{eq} + \frac{RT}{(1-\alpha)nF}ln\ (i_0) \qquad eq.S6$$

Downloaded from pubs.acs.org/ancac3/article-supplement/5429321/pdf/nn6c08876_si_001/ by CNR user on 21 September 2026

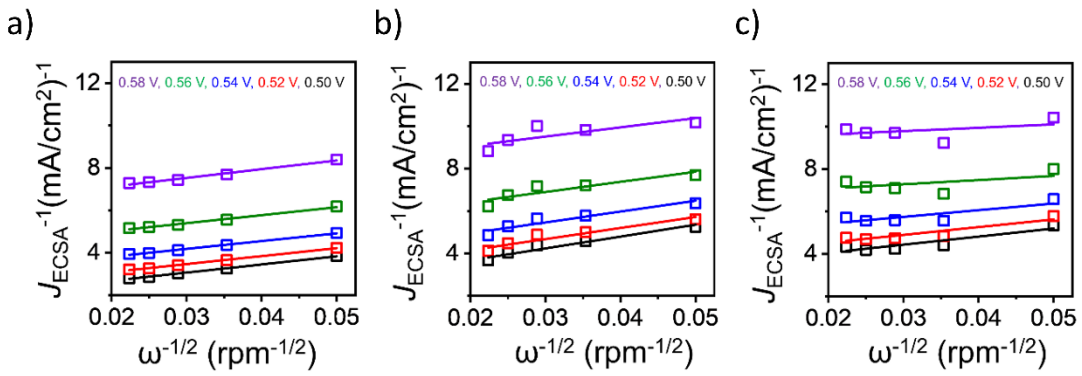

Figure S15. The Koutecky-Levich plots for a) L-MoS_2-III, b) L-MoS_2-I and c) Rac-MoS_2-III nanosheets

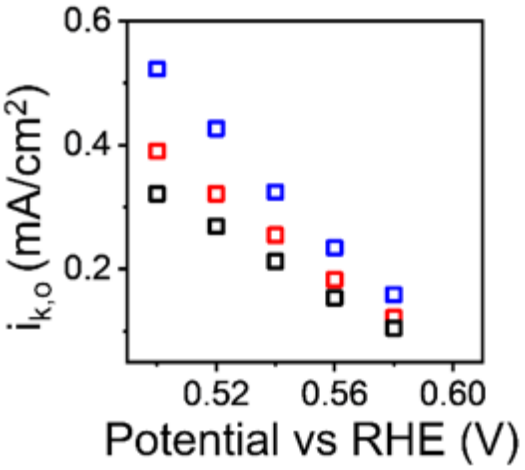

Figure S16. Kinetic current density against potentials selected for the Koutecky-Levich plot for L-MoS_2-III (blue), L-MoS_2-I (red) and Rac-MoS_2-III (black) nanosheets.

Table S4. Exchange current density (i_0) and the charge transfer coefficient (α) values:

Catalyst	α value for $n = 2$	α value for $n = 1$	i_0 (mA/cm^2)
L-MoS_2-III	0.8	0.6	7.5 x10^{-6}
L-MoS_2-I	0.8	0.6	5.3 x10^{-6}
Rac-MoS_2-III	0.8	0.6	4.5 x10^{-6}

Downloaded from pubs.acs.org/ancac3/article-supplement/5429321/pdf/nn6c08876_si_001/ by CNR user on 21 September 2026

Electrochemical impedance spectroscopy: Electrochemical impedance spectroscopy was employed to investigate the charge-transfer resistance of the chiral L-MoS_2-III and the racemic Rac-MoS_2-III catalysts at a bias potential of 1.70 V vs RHE within a frequency range of 0.01-100,000 Hz with an amplitude of 5 mV. Figure S17 shows that both catalysts have similar charge-transport resistance. The inset shows the equivalent electrical circuit used to fit the data, where R_u stands for the uncompensated solution resistance, R_{ct} for the charge transfer resistance at the electrode/electrolyte interface, R_p is the pseudo-resistance or resistance related to surface intermediates during the OER process, Q_{dl} is the charge accumulated at the electrode/electrolyte interface in the high frequency domain and Q_p represents the change in the charged surface species as OER proceeds. The charge transfer resistance for L-MoS_2-III is approximately 1167 ohm, well within the margin of error of rac-MoS_2-III (1205 ohm).

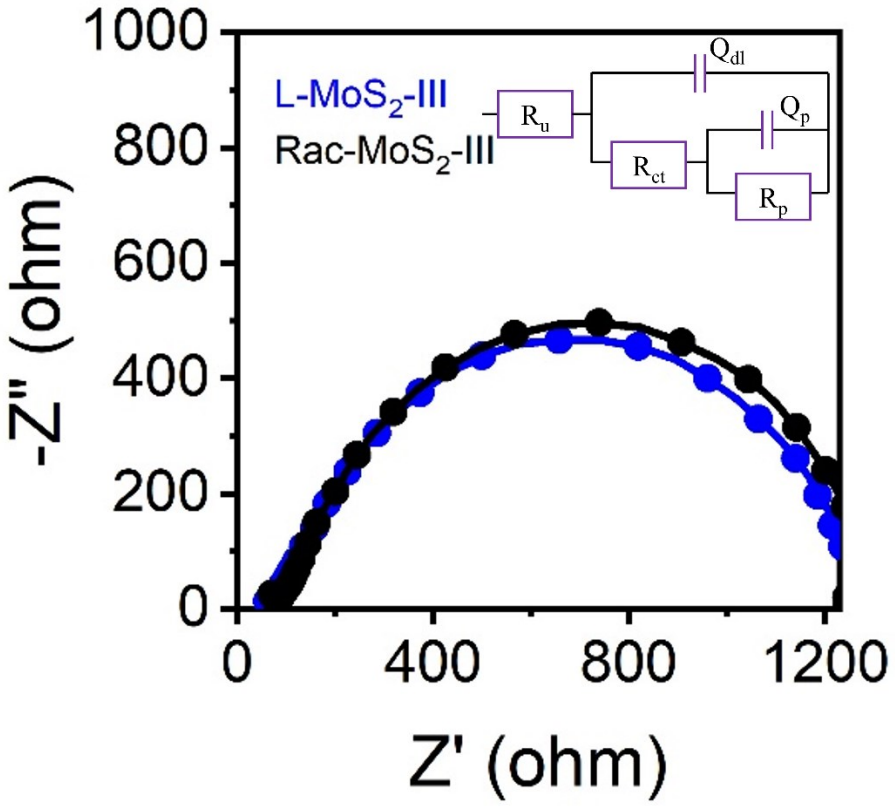

Figure S17. Shows Nyquist plots at a potential bias of 1.70 V vs RHE in the frequency range of 0.01-100000 Hz with 5 mV amplitude for the L-MoS_2-III (blue) and rac-MoS_2-III (black) catalysts. The inset shows the equivalent circuit used to fit the data.

Downloaded from pubs.acs.org/ancac3/article-supplement/5429321/pdf/nn6c08876_si_001/ by CNR user on 21 September 2026

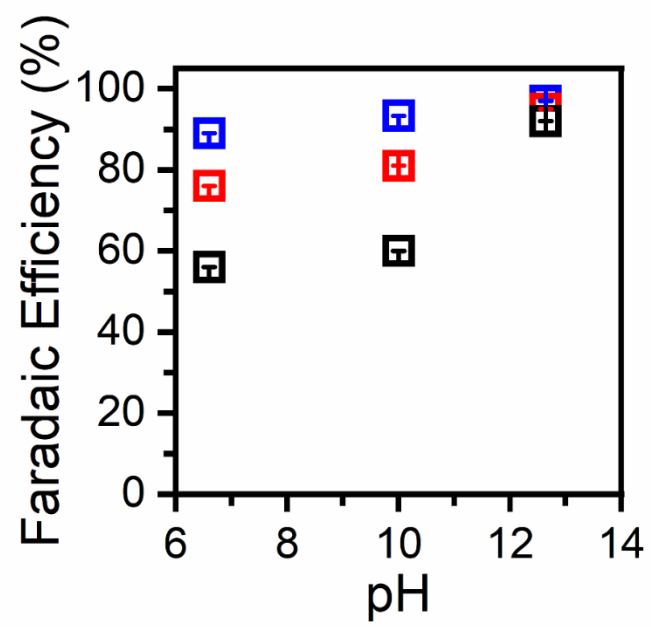

Figure S18. Faradaic efficiency plots for L-MoS_2-III (blue), L-MoS_2-I (red) and Rac-MoS_2-III (black) nanosheets in 0.1 M KOH (pH-12.6), 0.1 M K_2HPO_4 (pH -10.0) and 0.1 M Na_2SO_4 (pH – 6.7).

Downloaded from pubs.acs.org/ancac3/article-supplement/5429321/pdf/nn6c08876_si_001/ by CNR user on 21 September 2026

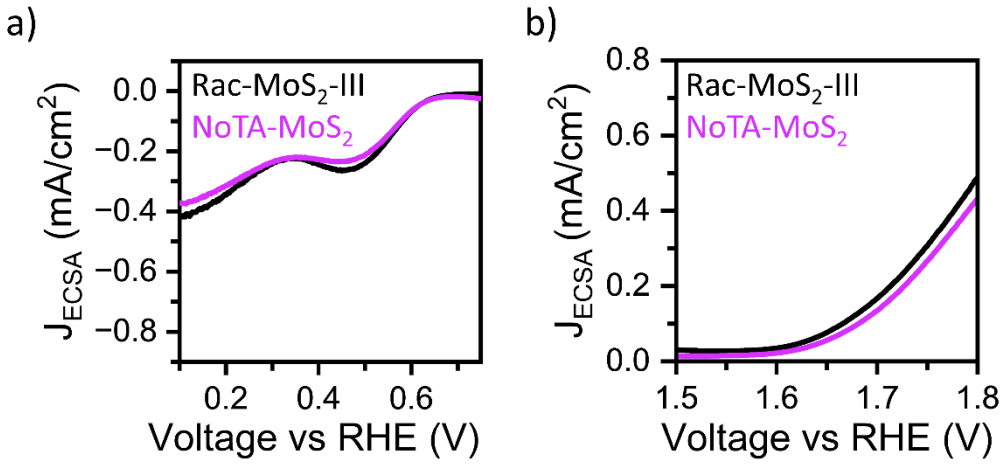

Figure S19. Comparison of the voltammograms of ORR (a) and OER (b) for Rac-MoS_2-III and NoTA-MoS_2 nanosheets used as achiral references.

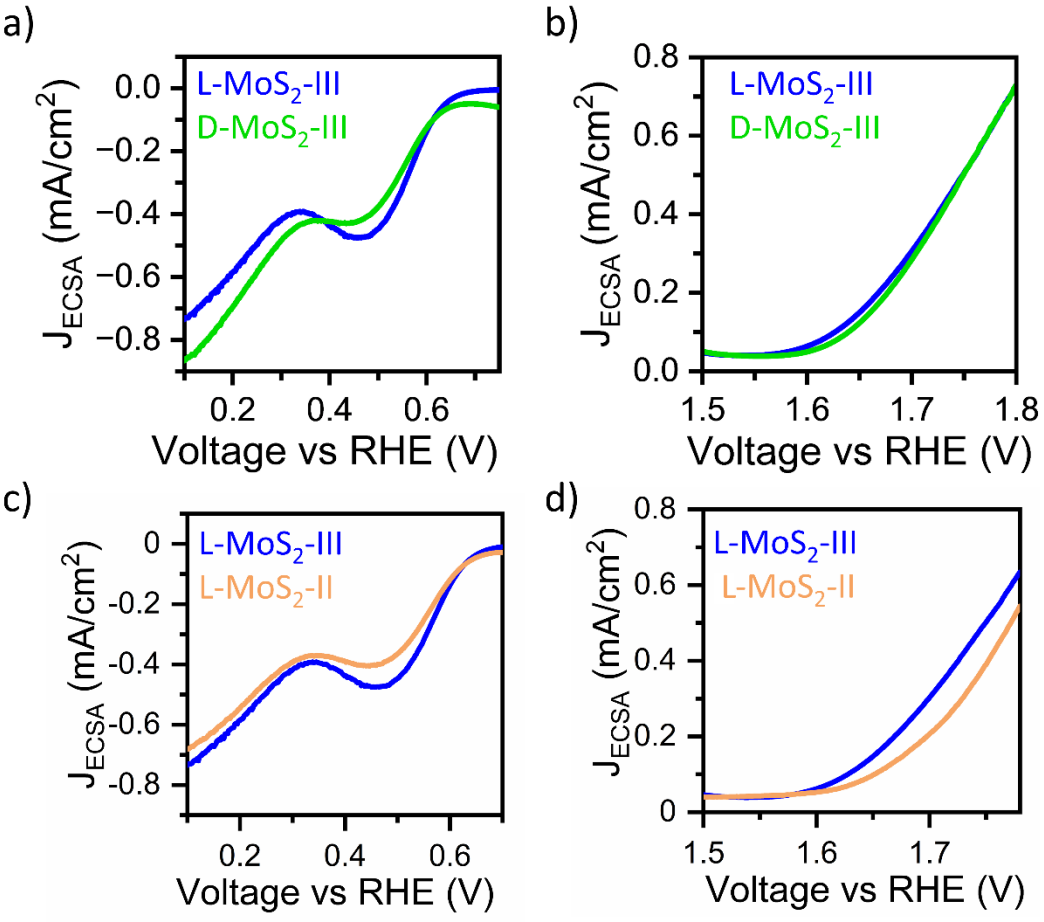

Figure S20. Comparison of the voltammograms of L-MoS_2-III with D-MoS_2-III and L-MoS_2-II nanosheets, ORR (a,c) and OER (b,d).

Downloaded from pubs.acs.org/ancac3/article-supplement/5429321/pdf/nn6c08876_si_001/ by CNR user on 21 September 2026

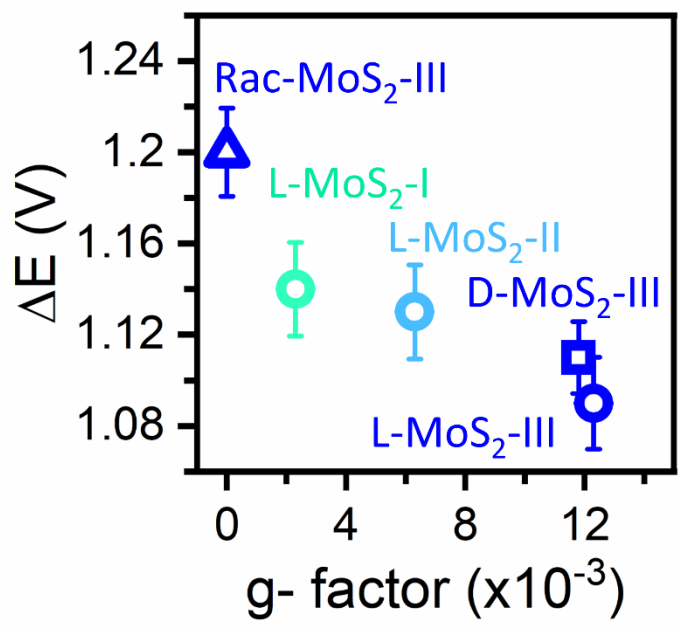

Figure S21. ORR/OER Potential gap quantified at current densities of -0.2 mA/cm^2 and 0.2 mA/cm^2 against the g-factor, L, D and Rac-nanosheets are represented as circles, squares and triangles, respectively.

Downloaded from pubs.acs.org/ancac3/article-supplement/5429321/pdf/nn6c08876_si_001/ by CNR user on 21 September 2026